optica

State-independent quantum tomography by photon-number-resolving measurements: supplementary material

RAJVEER NEHRA[1], AYE WIN[1,5], MILLER EATON[1], REIHANEH SHAHROKHSHAHI[1,4], NIRANJAN SRIDHAR[1,3], THOMAS GERRITS[2], ADRIANA LITA[2], SAE WOO NAM[2], AND OLIVIER PFISTER[1]

[1*]Department of Physics, University of Virginia, 382 McCormick Rd, Charlottesville, VA 22903, USA
[2]National Institute of Standards and Technology, 325 Broadway, Boulder, CO 80303, USA
[3]Now with Google, Inc., 1600 Amphitheatre Parkway, Mountain View, CA, USA
[4]Now with Xanadu, 372 Richmond Street West, Toronto, Ontario M5V1X6, Canada
[5]Now at: Department of Physics, University of Oklahoma, 440 W. Brooks St., Norman, OK 73019, USA
[*]Corresponding author: rn2hs@virginia.edu

Published 10 October 2019

This document provides supplementary information to "State-independent quantum tomography by photon-number-resolving measurements," https://doi.org/10.1364/OPTICA.6.001356. In Section 1 we provide an overview of our cavity-enhanced single-photon source. Section 2 discusses experimental calibrations and a model for loss analysis in the experiment.

1. CAVITY-ENHANCED NARROWBAND HERALDED SINGLE-PHOTON SOURCE

A. General model

Our single photon source is based on type-II spontaneous parametric downconversion (SPDC) in a periodically poled $KTiOPO_4$ (PPKTP) crystal. A pump photon at ω_p is downconverted into a cross-polarized signal-idler photon pair at $\omega_{s,i}$, such that $\omega_p = \omega_s + \omega_i$, and the presence of the signal photon is heralded by detecting the idler photon [1]. All tomographic measurements were therefore conditioned to the detection of an idler photon. The SPDC Hamiltonian is given by [2, 3]

$$H \propto i\hbar\chi^{(2)} \int d^3\vec{r}\, E_p^{(-)}(\vec{r},t) E_i^{(+)}(\vec{r},t) E_s^{(+)}(\vec{r},t) + H.c. \qquad \text{(S1)}$$

where $\chi^{(2)}$ is the crystal's nonlinearity and the fields in the Heisenberg picture take the form,

$$E_{j=p,s,i}^{(-)}(\vec{r},t) = E^{(+)}(\vec{r},t)^\dagger = \int d\omega_j\, A(\vec{r},\omega_j)\, \hat{a}_j\, e^{i[k_j(\omega_j)r - \omega_j t]}, \qquad \text{(S2)}$$

where $A(\vec{r},\omega_j)$ is an approximately slowly varying amplitude and $\hat{a}_j$ is the annihilation operator for the mode of frequency ω_j. Solving for the state under the evolution of the Hamiltonian in Eq. (S1) for low parametric gain regime and a non-depleted classical pump yields the output quantum state

$$|\psi\rangle = \int d^3\vec{k}_{s,i}\, d\omega_{s,i}\, \phi(\vec{k}_s,\omega_s,\vec{k}_i,\omega_i)\, \hat{a}_s^\dagger \hat{a}_i^\dagger\, |0\rangle_s\, |0\rangle_i \qquad \text{(S3)}$$

where $\phi(\vec{k}_s,\omega_s,\vec{k}_i,\omega_i)$ determines the spectral and spatial properties of the SPDC, depending on the pump field and the nonlinear crystal (phase matching bandwidth around $\vec{k}_p = \vec{k}_s + \vec{k}_i$). We can see from Eq. (S3) that the signal and idler photon pairs are emitted in a multitude of spatial and spectral modes. Therefore, any measurement on a particular idler mode will collapse the quantum state given by Eq. (S3) to a mixture of signal-mode states. As a result, the heralded signal state will not be a pure quantum state, which limits its applications in quantum information processing [4, 5]. This is because a nonzero vector phase-mismatch can lead to a detected, heralding idler photon with a "twin" signal photon completely out of alignment and therefore undetectable, even in the absence of losses, which greatly diminishes the experimentally accessible quantum correlations.

One therefore needs to emit photon pairs in the well defined spatial and spectral modes which are optimally coupled to the detectors. This involves spectral and spatial filtering and has been widely studied both theoretically and experimentally [6–11]. Our spectral and spatial filtering steps are discussed in the next section.

B. Spectral and spatial filtering

Spectral and spatial filtering was achieved by using optical resonators: both actively, by placing the nonlinear crystal in a resonant cavity — thereby building an optical parametric oscillator (OPO) — and passively, by using a filtering cavity (FC) and an interference filter (IF) after the OPO. The OPO was used in the well-below-threshold optical parametric amplifier (OPA) regime. The OPO cavity enhanced the SPDC at doubly resonant (signal and idler) frequencies by a factor of the square of the cavity finesse [12]. However, this enhancement was still masked by the "sea" of nonresonant SPDC photons until we filtered the idler with a short FC, which selected only one OPO mode, and with an IF, which selected only one of the FC modes. After filtering, we are allowed to consider the simpler OPA Hamiltonian

$$H = i\hbar\kappa\, \hat{a}_s^\dagger \hat{a}_i^\dagger + H.c., \tag{S4}$$

where κ is the product of the pump amplitude and $\chi^{(2)}$. This yields the well-known two-mode squeezed state

$$|\psi\rangle = (1-\zeta^2)^{\frac{1}{2}} \sum_{n=0}^{\infty} \zeta^n |n\rangle_s |n\rangle_i, \tag{S5}$$

where $\zeta = \tanh(\kappa t)$. In the weak pump regime, both κt and $\zeta \ll 1$, and Eq. (S5) can be approximated by

$$|\psi\rangle \simeq |0\rangle_s |0\rangle_i + \zeta |1\rangle_s |1\rangle_i + \mathcal{O}(\zeta^2) \tag{S6}$$

A detection of a single photon in the idler mode thus projects the signal mode into a single-photon state. Note that, since the heralding process consists in postselection of the idler channel, filtering losses in this channel are unimportant. Indeed, if the pump power is kept low enough that practically no pairs from different modes ever overlap in time, one can then reasonably claim that the detected, the heralded signal photon will be the twin of the filtered, heralding idler photon, as per Eq. (S6). It is important to also note that the situation will change if one seeks to herald a multi-photon state by using PNR detection for heralding, as per Eq. (S5). In that case, losses in the heralding channel cannot be tolerated as they will lead to errors.

2. EXPERIMENTAL CALIBRATIONS

A. Displacement calibration

The displacement operator was implemented by interfering the OPO signal mode with a phase- and amplitude-shifted coherent-state displacement field at a highly unbalanced beamsplitter with a reflectivity $r^2 = 0.97$. The interference visibility between the seed OPO beam and the displacement field was 90%. The amplitude shift $|\alpha|$ was effected by a homemade, temperature-stabilized electro-optic modulator consisting in an X-cut, 20 mm-long rubidium titanyl arsenate ($RbTiOAsO_4$) crystal; the phase shift $\arg(\alpha)$ was effected by a piezoelectric transducer-(PZT) actuated mirror. Both the EOM and the PZT mirror were driven by homemade, low-noise, high voltage drivers, fed by computer-controlled lock-in amplifiers.

The amplitude displacement was varied in 20 steps from $|\alpha| = 0$ to $|\alpha_{\max}| = 0.796(7)$, fixed by the TES' photon flux limit of 5 photons/μs. In order to probe the Wigner function over the whole phase space, one needs to have a maximum displacement amplitude of $|\alpha| = \sqrt{7}$, where the amplitude of the Wigner function drops down to 10^{-4}. It requires a PNR detector capable of counting a mean-photon number of $1 + |\alpha|^2 = 8$, where the probability to detect photon numbers at or above $n = 20$ is less than 10^{-4}. While our set-up only allows us to resolve up to 5 photon counts in the continuous-wave regime, due to pile-ups from our CW displacement field, other TES set-ups similar to ours have been characterized with resolution up to 17 photons in the pulsed regime [13].
The phase displacement was varied in 10 steps from 0 to 2π. The amplitude steps $|\alpha| = \sqrt{\eta}|\beta|$, where η is the overall detection efficiency, were directly calibrated by comparing the TES photon statistics to that of a Poisson distribution

$$P(n) = e^{-|\alpha|^2} \frac{|\alpha|^{2n}}{n!}, \tag{S7}$$

with the OPO beam blocked. This allowed us to determine the displacement amplitude

$$|\alpha| = \left[\frac{2P(2)}{P(1)}\right]^{\frac{1}{2}}. \tag{S8}$$

Note that this method requires the presence of 2-photon detection events, i.e., $|\alpha_{\min}| \simeq 0.15$ for the very first displacement amplitude, besides the zero displacement for which we blocked the displacement beam. Photon number statistics were averaged over 2 seconds to ensure an average calibration accuracy

$$\triangle|\alpha| = 3 \times 10^{-3} \tag{S9}$$

of the displacement amplitude. However, the error on the maximum displacement was somewhat larger

$$\triangle|\alpha_{\max}| = 7 \times 10^{-3}, \tag{S10}$$

due to the photon pileups occurring at higher flux which make the continuous-wave TES signals harder to analyze. We observed the long-term power stability of the laser to be on the order of 1% over an hour. The laser's short-term intensity noise was much lower as ensured by a built-in "noise eater" intensity servo. Moreover, the temperature stability of the EOM was on the order of 1 mK. Because of all this, we consider the error $\triangle|\alpha|$ on the displacement calibration to be valid over the course of our data acquisition time of several minutes. The phase steps were calibrated by scanning the interference fringe between the OPO seed beam and the displacement field, which provided a set of 10 voltage values for the PZT mirror. Experimental data runs were conducted by scanning the amplitude at fixed phases, with the phase PZT voltage being refreshed at every amplitude EOM voltage step. For each point of the quantum phase space, a continuous stream of data was acquired at 5 MS/s, digitized using an PCI board, and stored for subsequent photon statistical analysis. For each phase space coordinate, we acquired data for 3 seconds. As a result, for 10 phase and 20 amplitude scans the whole data acquisition duration was about 10 minutes.

A detailed discussion of our data analysis of continuous-wave photon counting can be found in our previous paper on coherent state tomography using PNR measurements [14].

B. Photon probability distributions versus displacement amplitude

Figure S1 displays the measured photon number distributions for a heralded single-photon input when $|\alpha| = 0$ (left) and 0.25 (right). For no displacement, the histogram reflects the exact same measurement as in Table 1 and Eq. 8 in the main text, and the result yields a compatible value of 0.58(2). The two-photon counts are essentially absent, which results in a very low second-order coherence $g^2(0) = 0.07(5)$. For $|\alpha| = 0.25$, the two-photon peak grows from the presence of the displacement field. In both cases, the observations agree with the theoretical distribution, calculated with η= 0.58. As expected, the single-

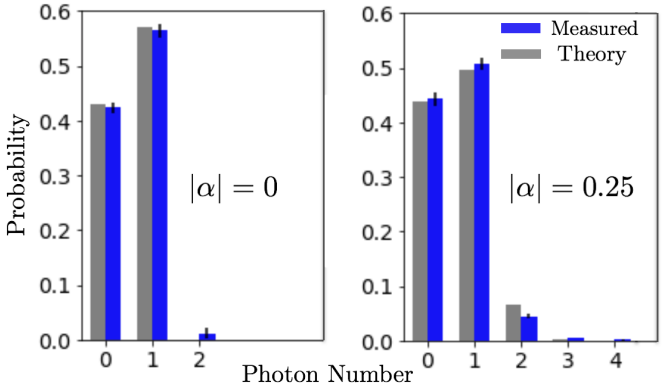

Fig. S1. Measured photon-number distributions, left: $\alpha = 0$ and right : $|\alpha| = 0.25$. Error bars (1σ) are calculated from the statistics of the measurements.

photon component decreased while the vacuum and higher photon components increased. It can be thought of as follows: If we displace a pure single-photon state, then we obtain

$$\hat{D}(\alpha)|1\rangle = \hat{D}(\alpha)\hat{a}^\dagger\hat{D}^\dagger(\alpha)|\alpha\rangle = \hat{a}^\dagger|\alpha\rangle - \alpha^*|\alpha\rangle.$$

Clearly, the first term has no vacuum component, as does the initial state $|1\rangle$, but the second term does have a vacuum component. Therefore, the displacement of a single-photon state increases its vacuum component probability amplitude, somewhat unintuitively. In the case where our initial state is a mixture of vacuum and single-photon, then it can be seen that for low enough displacement amplitudes, the vacuum component still increases from its previous value. As the displacement becomes large, the vacuum component will eventually decrease.

C. Model Wigner function and loss analysis

Before we turn to the tomography results, we outline the Wigner function model that accounts for the aforementioned nonideal system detection efficiency. There are several sources of losses in our experiment: photon absorption and general scattering out of the mode due to mismatch. As mentioned above, losses in the heralding channel can be factored out in the generation of a heralded single-photon state provided that the OPO output never contains more than one photon per mode during the detection window, which was the case in this work.

It is also important to note that the TES fiber is single-mode at telecom wavelengths but not at our operating wavelength of 1064 nm. Hence we need to address the possibility of multimode coupling into the TES fiber. A simple reasoning shows that this is not a matter of concern if there are no losses in the fiber. Indeed, the coupling of the input field into each of the different, orthogonal propagation modes of the fiber can be accurately described by as many beamsplitting operations into distinguishable outputs. While each of these beamsplitting operations does bring in vacuum fluctuations, all beamsplitter outputs are still detected and the final TES detection is simply that of the total photon number of all the fiber modes. In the absence of losses, the multimode fiber is a passive optical element which conserves the total photon number and the final total photon number measurement must therefore give the same exact result as the initial one, before the quantum light is coupled into the fiber. An argument could be made that fiber losses could be mode dependent, with higher-order modes being more likely to leak out of the fiber; we assume that this is negligible in our case because the operating wavelength was close enough to the specified single-mode wavelength that the mode order should not be that high.

We measured the coupling efficiency, η_{OFC}, into the TES fiber on the optical table by cleaving the fiber to insert a power meter and re-fusing it to the TES thereafter. To minimize the coupling to higher modes, we optimized our fiber coupling to as high as 90% with the seed beam (discussed in the "spectral and spatial filtering" section above) and we also measured the intensity variations of about one percent at the output of the fiber. This ensures that most of the fiber coupling was to the fundamental mode of the fiber. However, we didn't measure the overall fiber transmission into the TES cryostat. This was bundled with the TES quantum efficiency in η_{TES}, which was inferred from all other measured efficiencies, as summarized in Table S1. We modeled

η_{TES}	η_{OT}	η_{BS}	η_{OFC}	η
0.71(3)	0.93(1)	0.97(1)	0.90(2)	0.58(2)

Table S1. η_{TES}: TES quantum efficiency (including fiber transmissivity); η_{OT} : optical transmission of single-photon signal field from the OPO to the displacement operation; η_{BS}: displacement beamsplitter transmissivity; η_{OFC}: optical fiber coupling. The overall efficiency $\eta = \eta_{\mathrm{TES}} \times \eta_{\mathrm{OT}} \times \eta_{\mathrm{BS}} \times \eta_{\mathrm{OFC}}$.

losses by considering a fictitious beamsplitter of transmissivity η and reflectivity $(1-\eta)$, placed between the displacement and a detector of unity efficiency as shown in Fig.S2. The input state of this system is

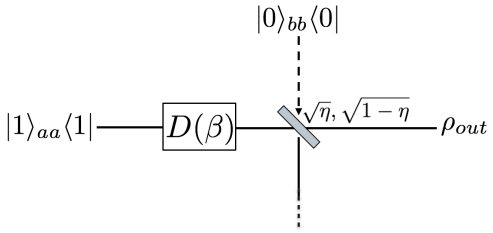

Fig. S2. Loss model. The beamsplitter transmission and reflection coefficients are $\sqrt{\eta}$ and $\sqrt{1-\eta}$ respectively.

$$\hat{\rho}_{\mathrm{in}} = |1\rangle_{a\,a}\langle 1| \otimes |0\rangle_{b\,b}\langle 0|. \tag{S11}$$

After applying the displacement $\hat{D}_a(\beta)$ and beamsplitter $\hat{U}_{ab}$ operators we obtain the reduced, detected density operator by

tracing out the vacuum mode

$$\hat{\rho}_{\text{out}} = \text{Tr}_b \left[\hat{U}_{ab} \hat{D}(\beta) |1\rangle_{a\,a}\langle 1| \otimes |0\rangle_{b\,b}\langle 0| \hat{D}^\dagger(\beta) \hat{U}_{ab}^\dagger \right] \quad \text{(S12)}$$

$$= \hat{D}(\sqrt{\eta}\beta) \left[\eta |1\rangle_{a\,a}\langle 1| + (1-\eta)|0\rangle_{a\,a}\langle 0| \right] \hat{D}(\sqrt{\eta}\beta)^\dagger. \quad \text{(S13)}$$

From Eq. (S13) we can see that displacement by β followed by losses η is essentially the same as introducing losses first by mixing the pure single-photon state with vacuum, and then applying a displacement by the reduced amount $\sqrt{\eta}\beta$. Due to the linearity of the Wigner function, Eq. (S13) shows that the experimentally reconstructed Wigner function will in fact be

$$W(q,p) = \eta W_{|1\rangle\langle 1|}(q,p) + (1-\eta) W_{|0\rangle\langle 0|}(q,p). \quad \text{(S14)}$$

As expected, losses (1-η) add a Gaussian vacuum function to the original nonpositive Wigner function of the single-photon state. In particular, the undisplaced photon-number distribution will yield the overall transmissivity of the whole experiment η, as in Fig.S1, left.

REFERENCES

1. A. I. Lvovsky, H. Hansen, T. Aichele, O. Benson, J. Mlynek, and S. Schiller, "Quantum state reconstruction of the single-photon Fock state," Phys. Rev. Lett. **87**, 050402 (2001).
2. W. P. Grice and I. A. Walmsley, "Spectral information and distinguishability in type-ii down-conversion with a broadband pump," Phys. Rev. A **56**, 1627–1634 (1997).
3. A. Christ and C. Silberhorn, "Limits on the deterministic creation of pure single-photon states using parametric down-conversion," Phys. Rev. A **85**, 023829 (2012).
4. N. Gisin and R. Thew, "Quantum communication," Nat. Photonics **1**, 165 (2007).
5. J. F. Clauser and A. Shimony, "Bell's theorem. Experimental tests and implications," Rep. Prog. Phys. **41**, 1881 (1978).
6. Z. Y. Ou and Y. J. Lu, "Cavity enhanced spontaneous parametric down-conversion for the prolongation of correlation time between conjugate photons," Phys. Rev. Lett. **83**, 2556–2559 (1999).
7. Y. Jeronimo-Moreno, S. Rodriguez-Benavides, and A. B. U'Ren, "Theory of cavity-enhanced spontaneous parametric downconversion," Laser Phys. **20**, 1221–1233 (2010).
8. S. Virally, S. Lacroix, and N. Godbout, "Limits of heralded single-photon sources based on parametric photon-pair generation," Phys. Rev. A **81**, 013808 (2010).
9. M. Scholz, L. Koch, R. Ullmann, and O. Benson, "Single-mode operation of a high-brightness narrow-band single-photon source," Appl. Phys. Lett. **94**, 201105 (2009).
10. D. Höckel, L. Koch, and O. Benson, "Direct measurement of heralded single-photon statistics from a parametric down-conversion source," Phys. Rev. A **83**, 013802 (2011).
11. X.-H. Bao, Y. Qian, J. Yang, H. Zhang, Z.-B. Chen, T. Yang, and J.-W. Pan, "Generation of narrow-band polarization-entangled photon pairs for atomic quantum memories," Phys. Rev. Lett. **101**, 190501 (2008).
12. C. E. Kuklewicz, E. Keskiner, F. N. C. Wong, and J. H. Shapiro, "A high-flux entanglement source based on a doubly resonant optical parametric amplifier," J. Opt. B: Quantum Semiclass. Opt. **4**, S162–S168 (2002).
13. P. C. Humphreys, B. J. Metcalf, T. Gerrits, T. Hiemstra, A. E. Lita, J. Nunn, S. W. Nam, A. Datta, W. S. Kolthammer, and I. A. Walmsley, "Tomography of photon-number resolving continuous-output detectors," New J. Phys. **17**, 103044 (2015).
14. N. Sridhar, R. Shahrokhshahi, A. J. Miller, B. Calkins, T. Gerrits, A. Lita, S. W. Nam, and O. Pfister, "Direct measurement of the Wigner function by photon-number-resolving detection," J. Opt. Soc. Am. B **31**, B34–B40 (2014).